Effective $S = 2$ antiferromagnetic spin chain in the salt (o-MePy-V)$FeCl_4$

Y. Iwasaki,[1,*] T. Kida,[2] M. Hagiwara,[2] T. Kawakami,[3] Y. Hosokoshi,[1] Y. Tamekuni,[1] and H. Yamaguchi[1,†]

[1]*Department of Physical Science, Osaka Prefecture University, Osaka 599-8531, Japan*

[2]*Center for Advanced High Magnetic Field Science (AHMF), Graduate School of Science, Osaka University, Osaka 560-0043, Japan*

[3]*Department of Chemistry, Osaka University, Toyonaka, Osaka 560-0043, Japan*

(Received 20 November 2017; revised manuscript received 29 December 2017; published 8 February 2018)

We present a model compound for the $S = 2$ antiferromagnetic (AF) spin chain composed of the salt (o-MePy-V)$FeCl_4$. *Ab initio* molecular-orbital calculations indicate the formation of a partially stacked two-dimensional (2D) spin model comprising five types of exchange interactions between $S = 1/2$ and $S = 5/2$ spins, which locate on verdazyl radical and Fe ion, respectively. The magnetic properties of the synthesized crystals indicate that the dominant interaction between the $S = 1/2$ and $S = 5/2$ spins stabilizes an $S = 2$ spin in the low-temperature region, and an effective $S = 2$ AF chain is formed for $T \ll 10$ K and $H < 4$ T. We explain the magnetization curve and electron-spin-resonance modes quantitatively based on the $S = 2$ AF chain. At higher fields above quantitatively 4 T, the magnetization curve assumes two-thirds of the full saturation value for fields between 4 and 20 T, and approaches saturation at ∼40 T. The spin model in the high-field region can be considered as a quasi-2D $S = 1/2$ honeycomb lattice under an effective internal field caused by the fully polarized $S = 5/2$ spin.

DOI: 10.1103/PhysRevB.97.085113

I. INTRODUCTION

The diversity of possible molecular arrangements in organic materials is expected to facilitate the design of a wide range of magnetic materials with interesting properties. In fact, since the discovery of the first organic ferromagnet [1], a large number of organic radical materials have been synthesized over the past two decades through the use of representative nitroxide-type radicals [2]. In order to realize the next stage of material design, we have focused our attention on the verdazyl radical, which can exhibit a delocalized π-electron spin density even in nonplanar molecular structures. Moreover, the flexibility of the molecular orbitals in the verdazyl radical enables the tuning of intermolecular magnetic interactions through molecular design. Recently, we demonstrated that the verdazyl radical can form a variety of unconventional spin systems, including the ferromagnetic-leg ladder, quantum pentagon, and random honeycomb, which have not been realized in conventional inorganic materials [3–7]. Furthermore, we succeeded in combining our verdazyl radicals with 3d transition metals [8,9], and demonstrated that the strong coupling between the metal and verdazyl radical spins results in the formation of a hybrid spin in low-temperature regions, producing an unprecedented type of $S > 1/2$ spin system [9]. Such metal-radical hybrid spins are essential to the formation of the effective $S = 2$ model presented in this work.

The study of half-integer and integer spin chains has also brought about an important topic of research in recent decades. Haldane's unexpected prediction related to a gap between the ground and excited states of integer Heisenberg spin systems in 1983 [10] stimulated many experimental and theoretical studies focused on the qualitative differences between antiferromagnetic (AF) half-integer and integer Heisenberg spin chains. While subsequent studies of integer $S = 1$ spin systems have established the presence of the predicted Haldane gap [11–14], there are remarkably few examples of $S > 1$ 1D spin systems. It was also shown in the $S = 1$ case that the ground state below the Haldane gap can be effectively described as a valence-bond solid [15,16], in which each integer spin is considered as two half-integer spins forming a singlet state between different sites. However, there are only a few examples of the next group of integer spin systems with $S = 2$ [17–23], and their intrinsic behavior has yet to be fully clarified. In particular, the Haldane state for actual $S > 1$ spin systems has not been realized, but ordered magnetic states were observed instead due to the large magnetic moments and interchain interactions in the known examples of $S = 2$ spin systems. The effective $S = 2$ AF chain discussed in the present work also exhibits an ordered state arising from the same origins.

In this work, we report our results from a model compound characterized by an effective $S = 2$ AF spin chain. We successfully synthesized single crystals of the verdazyl-based salt (o-MePy-V)$FeCl_4$ [o-MePy-V = 3-(2-methylpyridyl)-1,5-diphenylverdazyl]. *Ab initio* molecular orbital (MO) calculations indicated the formation of a partially stacked two-dimensional (2D) spin model composed of five different types of interactions between $S = 1/2$ and $S = 5/2$ spins, which locate on verdazyl radical and Fe ion, respectively. Magnetic susceptibility, specific heat, magnetization, and electron-spin-resonance (ESR) measurements were conducted in order to study the properties of the synthesized crystals. The resulting magnetic properties indicated that the dominant interaction between the $S = 1/2$ and $S = 5/2$ spins stabilizes a hybrid $S_{hy} = 2$ spin at low temperatures, forming an effective $S = 2$ AF chain for $T \ll 10$ K and $H < 4$ T. In particular, the magnetization curve and ESR resonance modes are well

*iwasaki@p.s.osakafu-u.ac.jp

†yamaguchi@p.s.osakafu-u.ac.jp

described by the $S = 2$ AF spin chain. At higher fields above quantitatively 4 T, the magnetization is two-thirds of the full saturation for the fields between 4 and 20 T, and approaches saturation at approximately 40 T.

II. EXPERIMENTAL AND NUMERICAL METHOD

We synthesized *o*-MePy-V using a conventional procedure [24] and prepared an iodide salt of the radical cation (o-MePy-V)I using a reported procedure for salts with similar chemical structures [25]. 1-butyl-3-methylimidazolium tetrachloroferrate (132 mg, 0.39 mmol) was slowly added to a solution of (*o*-MePy-V)I (127 mg, 0.28 mmol) in 50 ml of methanol and stirred for 1 h. The dark-red solid (*o*-MePy-V)$FeCl_4$ was then separated by filtration and washed with methanol. The dark-red residue was recrystallized using acetonitrile.

The crystal structure was determined on the basis of intensity data collected using a Rigaku AFC-8R Mercury CCD RA-Micro7 diffractometer with Japan Thermal Engineering XR-HR10K. The magnetizations were measured using a commercial superconducting quantum interference device magnetometer (MPMS-XL, Quantum Design). High-field magnetization measurement in pulsed magnetic fields of up to approximately 53 T was conducted using a nondestructive pulse magnet. The experimental results were corrected for the diamagnetic contribution of -2.8×10^{-4} emu mol^{-1} calculated by the Pascal method. The specific heat was measured with a commercial calorimeter (PPMS, Quantum Design) using a thermal relaxation method. The ESR measurements were performed utilizing a vector network analyzer (ABmm) and a superconducting magnet (Oxford Instruments). At approximately 20.6, 27.5, and 34.1 GHz, we used laboratory-built cylindrical high-sensitivity cavities. *X*-band (9.47 GHz) ESR measurements were conducted using a Bruker EMX-Plus spectrometer. All above the experiments were performed using small, randomly oriented single crystals with typical dimensions of $0.5\times0.1\times0.1$ mm^3.

Ab initio MO calculations were performed using the UB3LYP method with the basis set 6-31$G(d,p)$ in the Gaussian 09 program package. For the estimation of intermolecular magnetic interaction, we applied our evaluation scheme that have been studied previously [26].

Our Monte Carlo (MC) calculations were performed using a standard Metropolis method with a 256-site system and periodic boundary conditions. It was subsequently confirmed that the system did not exhibit any size dependent effects. Each MC run was performed after discarding the initial 20 000 MC steps per spin (MCS), with a subsequent 180 000 MCS run to ensure the system reached its equilibrium.

III. RESULTS AND DISCUSSION

A. Crystal structure and magnetic model

The crystallographic data for the synthesized (*o*-MePy-V)$FeCl_4$ are summarized in Table I, and the molecular structure is shown in Fig. 1(a). The verdazyl ring (which includes four N atoms), the upper two phenyl rings, and the bottom methylpyridyl ring are labeled R_1, R_2, R_3, and R_4, respectively. The dihedral angles of R_1-R_2, R_1-R_3, R_1-R_4 are approximately 25°, 19°, and 20°, respectively. The results of the MO calculations indicate that approximately 59% of the total spin density is present on R_1. Further, while R_2 and R_3 each account for approximately 19% and 18% of the relatively large total spin density, R_4 accounts for less than 4% of the total spin density. Therefore, the intermolecular interactions are caused by the short contacts related to the R_1, R_2, and R_3 rings. Note that, because this study focuses on the low-temperature magnetic properties, the crystallographic data obtained at 25 K are used hereafter.

TABLE I. Crystallographic data for (o-MePy-V)$FeCl_4$.

Formula	$C_{20}H_{19}Cl_4FeN_5$	
Crystal system	monoclinic	
Space group	$P2_1/c$	
Temperature (K)	RT	25(2)
Wavelength (Å)	0.7107	
a (Å)	7.666(3)	7.421(6)
b (Å)	18.965(7)	18.860(16)
c (Å)	15.759(6)	15.702(14)
β (deg)	95.853(6)	95.972(14)
V (Å^3)	2279.2(15)	2186(3)
Z	4	
D_{calc} (g cm^{-3})	1.536	1.602
Total reflections	3519	3577
Reflection used	2073	2975
Parameters refined	272	
R $[I > 2\sigma(I)]$	0.0731	0.0650
R_w $[I > 2\sigma(I)]$	0.1748	0.1489
Goodness of fit	1.061	1.054
CCDC	1 585 718	1 585 719

The *o*-MePy-V and $FeCl_4$ molecules of the synthesized crystal have $S_V = 1/2$ and $S_{Fe} = 5/2$, respectively. The *ab initio* MO calculations were performed in order to evaluate the exchange interaction between the spins, and five types of dominant interactions were found between the *o*-MePy-V and $FeCl_4$ molecules, as shown in Figs. 1(b)–1(f). They are evaluated as $J_1/k_B = 6.4$ K, $J_2/k_B = 3.9$ K, $J_3/k_B = 12.3$ K, $J_4/k_B = -6.2$ K, and $J_5/k_B = -4.4$ K, which are defined in the Heisenberg spin Hamiltonian given by $\mathcal{H} = J_n\sum_{\langle i,j\rangle}\boldsymbol{S}_i\cdot\boldsymbol{S}_j$, where $\sum_{\langle i,j\rangle}$ denotes the sum over the neighboring spin pairs. The J_1 and J_2 describe the coupling between the *o*-MePy-V and $FeCl_4$ molecules, as shown in Figs. 1(b) and 1(c). The molecular pairs associated with the J_3, J_4, and J_5 are between *o*-MePy-V molecules, and are related through their inversion center for the J_3 and J_5, and through a *c*-glide symmetry for the J_4, as shown in Figs. 1(d)–1(f), respectively. We note that intermolecular interactions between organic radical and 3*d* transition-metal anions tend to be underestimated, while the calculated estimates of the coupling between verdazyl radicals exhibits high reliability [27–29]. As shown in Fig. 1(g), the molecular pairs associated with the J_1, J_2, J_3, and J_4 couple two dimensionally in the *bc* plane, and are partially connected by the ferromagnetic interaction J_5, as shown in Fig. 1(h). A 2D spin model composed of the J_1, J_2, J_3, and J_4 with $S_V = 1/2$ and $S_{Fe} = 5/2$ in the *bc* plane is presented in Fig. 2(a). The J_3 and J_4 form a honeycomb lattice of $S_V = 1/2$, and the J_5 corresponds to the interaction between honeycomb lattices. Following analysis of the magnetic susceptibility indicates

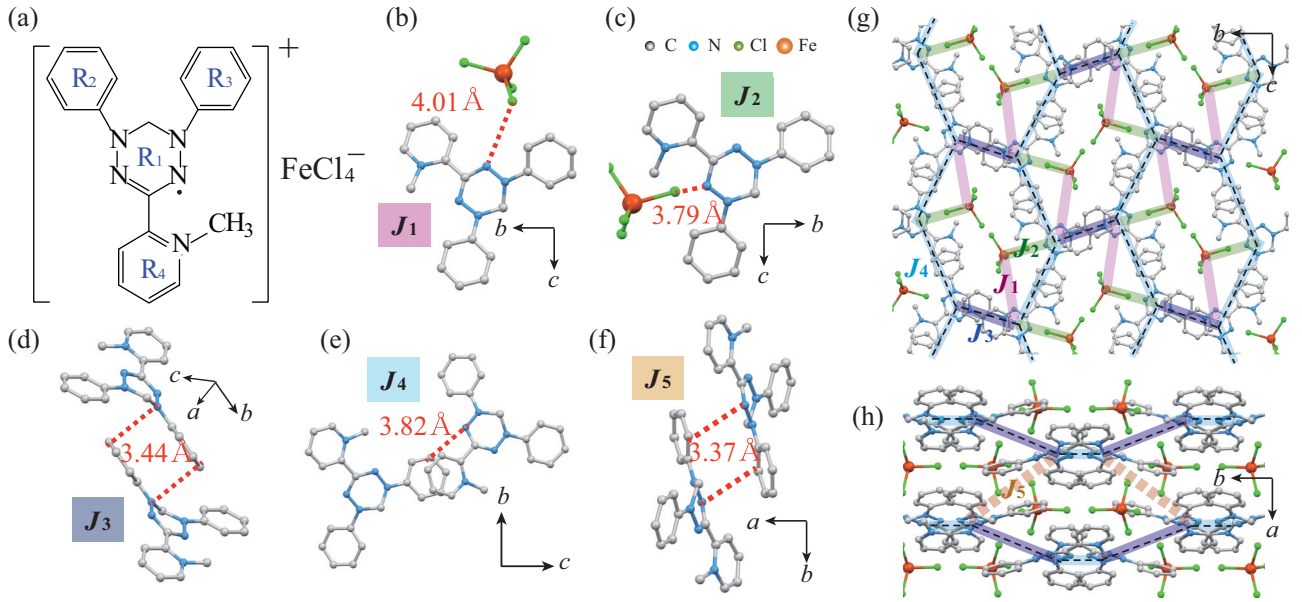

FIG. 1. (a) Molecular structure of (*o*-MePy-V)$FeCl_4$. Molecular pairs associated with exchange interactions (b) J_1, (c) J_2, (d) J_3, (e) J_4, and (f) J_5. Hydrogen atoms are omitted for clarity. The broken lines indicate short contact related to the rings with high spin-density distributions. Crystal structure in the (g) *bc* and (h) *ab* planes. The broken lines represent the honeycomb lattice composed of J_3 and J_4.

that the S_V and a part of the S_{Fe} spins form a nonmagnetic state through the AF coupling J_1, yielding the $S_{hy} = 2$. Thus, the dominant interaction between $S_{hy} = 2$ spins is expected to have an exchange path composed of $S_{Fe} - S_V - S_{Fe}$ instead of $S_{Fe} - S_V - S_V - S_{Fe}$. Because the interactions J_3, J_4, and J_5 correspond to the exchange path of $S_V - S_V$, they do not contribute to the effective interactions in the low-temperature region. Accordingly, in the low-temperature region, the J_1 and J_2 between the *o*-MePy-V and $FeCl_4$ molecules form a 1D spin chain, as shown in Fig. 2(b), and are key to our following understanding of the effective $S = 2$ chain.

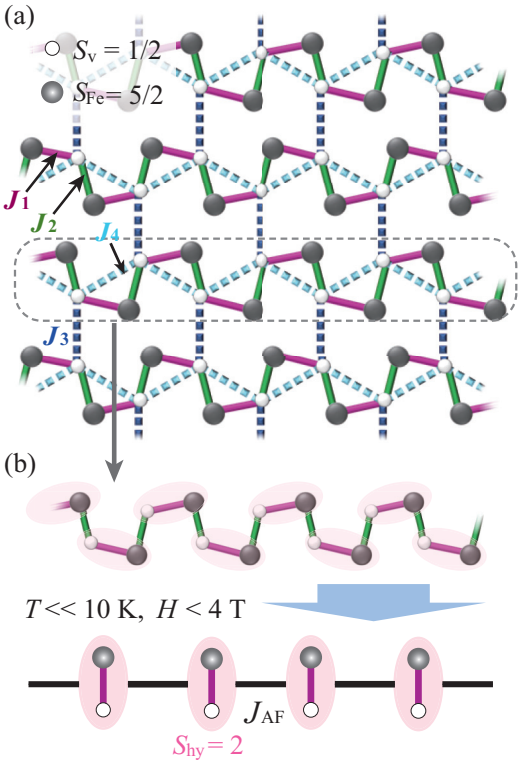

FIG. 2. (a) 2D spin model composed of J_i (i = 1–4) with $S_V = 1/2$ and $S_{Fe} = 5/2$. (b) 1D chain composed of exchange path of S_{Fe}-S_V-S_{Fe} (J_1-J_2) and effective $S_{hy} = 2$ AF chain.

B. Magnetic susceptibility

Figure 3 shows the temperature dependence of the magnetic susceptibility ($\chi = M/H$) at 0.1 and 1.0 T. We observe an anomalous change in the temperature dependence at 5.2 K, below which a significant difference between 0.1 and 1.0 T appears. This behavior indicates that a phase transition to

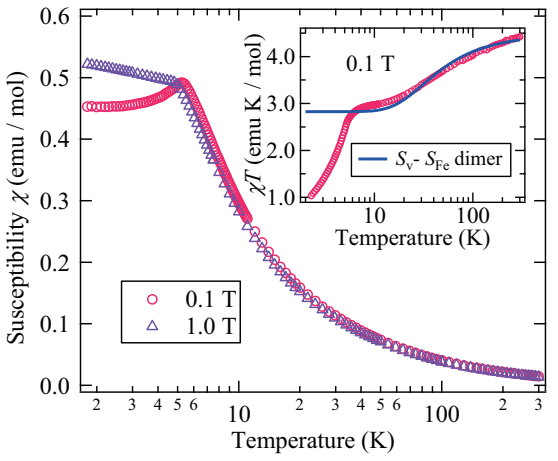

FIG. 3. Temperature dependence of magnetic susceptibility ($\chi = M/H$) of (*o*-MePy-V)$FeCl_4$ at 0.1 and 1.0 T. The inset shows the temperature dependence of χT. The solid line represents the calculated result for the S_V-S_{Fe} dimer coupled by J_1.

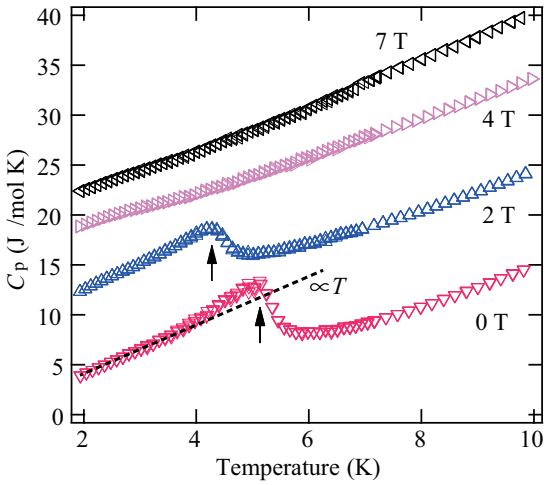

FIG. 4. Specific heat of (o-MePy-V)$FeCl_4$ at 0, 2, 4, 7 T. The arrows indicate the phase-transition temperatures. For clarity, the values for 2, 4, and 7 T have been shifted up by 8.5, 16, 21 J mol^{-1} K, respectively.

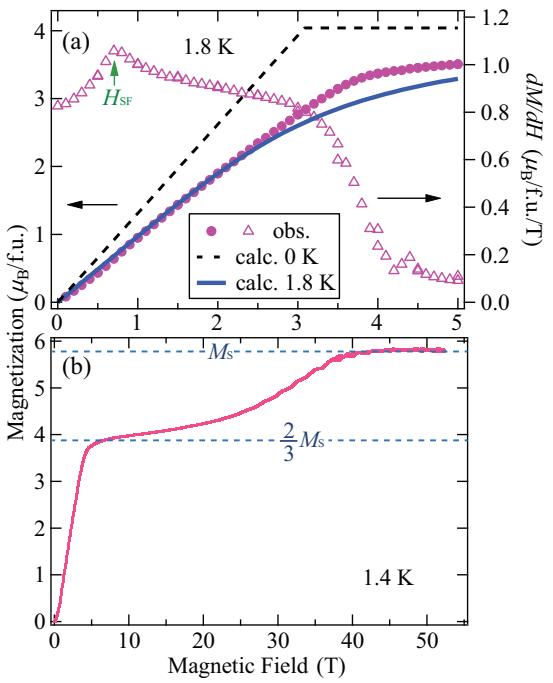

FIG. 5. Magnetization curve of (o-MePy-V)$FeCl_4$ (a) below 5 T at 1.8 K and (b) up to 53 T at 1.4 K. The broken and solid lines represent the calculated result for the $S = 2$ AF chain with $J_{AF}/k_B = 0.52$ K at 0 and 1.8 K, respectively. The arrow indicates sharp peak of dM/dH associated with the spin-flop transition at H_{SF}. The horizontal lines indicate full saturation M_s and $2/3M_s$ considering the sample purity of 96%.

a three-dimensional (3D) long-range order (LRO) occurs at $T_N = 5.2$ K. In the higher-temperature region, the value of χT decreases with decreasing temperature and becomes approximately constant around 10 K, as shown in the inset of Fig. 3. The approximately constant χT value is very close to the Curie constant of 3.0 emu K/mol for an $S = 2$ noninteracting spin, and suggests the formation of a hybrid spin $S_{hy} = 2$ through the strong coupling between $S_V = 1/2$ and $S_{Fe} = 5/2$ spins. We then calculated χT for the S_V-S_{Fe} single dimer coupled by the AF J_1, obtaining a good agreement between experiment and calculation above ~10 K for $J_1/k_B = 17.7$ K, $g = 2.0$, and a sample purity of 96%. As the calculated value of J_1 is about 2.8 times larger than that resulting from the MO evaluation, the difference implies that the second interaction between the o-MePy-V and $FeCl_4$ molecules (i.e., J_2) should also be larger than the outputted value from the MO evaluation. The value of χT also decreases with decreasing temperature below 10 K, which indicates further contributions from interactions between the hybrid spins. Since the S_V and a part of the S_{Fe} spins form a nonmagnetic state through the AF coupling J_1 in the hybrid spin, the dominant interaction between the $S_{hy} = 2$ spins is expected to have an exchange path of $S_{Fe} - S_V - S_{Fe}$ instead of $S_{Fe} - S_V - S_V - S_{Fe}$. Such interactions correspond to the coupling between the o-MePy-V and $FeCl_4$ molecules and form a 1D chain, as shown in Fig. 2(b). In accordance with these results, the hybrid spins composed of the $S_V = 1/2$ and $S_{Fe} = 5/2$ spins can be viewed as connected by an effective interaction J_{AF} (given by an exchange path related to J_2) and form an $S_{hy} = 2$ AF chain in the low-temperature region below 10 K, as shown in Fig. 2(b).

C. Specific heat

The experimental results for the specific heat C_p at zero-field clearly exhibit a λ-type sharp peak at T_N, which is associated with the phase transition to the LRO, as shown in Fig. 4. In the low-temperature region below ~4 K, the C_m shows clear T-linear behavior that is attributed to a linear dispersive mode in 1D AF systems [30,31], as is the case with T^2 behavior in the 2D AF system [27]. This behavior indicates that the system discussed in this work has a quasi-1D character, yielding a sufficient development of the short-range order (SRO) in the effective 1D chain above T_N. In magnetic fields, the phase-transition temperature decreases with increasing fields and almost disappears above 4 T, as shown in Fig. 4. The disappearance of this phase transition is consistent with the formation of a fully polarized state in the effective AF chain, as shown in the following magnetization curve.

D. Magnetization curve

As shown in Fig. 5(a), the magnetization curve increases linearly with increasing field up to approximately 4 T. This low-field gradual increase is completely different from the concave shape of magnetization curves in general quantum spin systems, in which quantum fluctuations are suppressed by the application of magnetic fields, yielding a rapid increase of magnetization [27–29]. The linear increase observed here indicates that the magnetic properties in the low-temperature and low-field regions can be described by classical systems with large spins, which is consistent with the formation of an effective $S_{hy} = 2$ AF chain. We then calculated the magnetization curve based on the $S = 2$ AF chain using the classical MC method. The spin Hamiltonian is expressed as

$$\mathcal{H} = J_{AF}\sum_{\langle ij\rangle} \boldsymbol{S}_i \cdot \boldsymbol{S}_j - g\mu_B H \sum_i \boldsymbol{S}_i, \qquad (1)$$

where $\boldsymbol{S}$ is the spin operator, g is the g factor, $g = 2.02$ from ESR, μ_B is the Bohr magneton, and H is the external magnetic field. We obtained good agreement between the experimental and calculated results using $J_{\mathrm{AF}}/k_{\mathrm{B}} = 0.52$ K, as shown in Fig. 5(a). Moreover, the magnetization curve at $T = 0$ that was determined using a mean-field approximation is shown to reach saturation at approximately 3 T. Thus, the gradual increase at 1.8 K can be attributed to the effect of temperature fluctuations. Since the calculations presented here were based on the finite 1D system, deviations near the saturation point should originate from real 3D effects accompanying the phase transition. In terms of the field derivative of the magnetization, we observe a distinct peak at approximately $H_{\mathrm{SF}} \simeq 0.65$ T, as shown in Fig. 5(a). This indicates a spin-flop transition that is caused by a small magnetic anisotropy.

At higher fields, the magnetization assumes two-thirds of the full saturation value for fields between 4 and 20 T, before increasing again toward the saturation at approximately 40 T, as shown in Fig. 5(b). This 2/3-plateaulike behavior corresponds to the saturation of the effective $S_{\mathrm{hy}} = 2$ AF chain, in which the $S_{\mathrm{Fe}} = 5/2$ spins are fully polarized along the field direction. Therefore, the effective spin model in the high-field region can be considered as an $S_{\mathrm{V}} = 1/2$ honeycomb lattice composed of J_3, J_4 with interplane interaction J_5. In such spin model, an effective internal field, which increases the saturation field, is arising from the fully polarized $S_{\mathrm{Fe}} = 5/2$ spins through AF J_1 and J_2. Indeed, the magnetization curve exhibits a nonlinear increase associated with the quantum spin $S_{\mathrm{V}} = 1/2$ and a high saturation field compared to the expected energy scale of the interactions forming the quasi-2D honeycomb lattice.

E. Electron-spin resonance

The frequency dependence of the ESR absorption spectra in the ordered phase is presented in Figs. 6(a) and 6(b). As shown in Fig. 6(a), the resonance signals at high frequencies are almost proportional to the external field. Conversely, those at low frequencies in Fig. 6(b) exhibit broad signals with a number of resonance fields and obviously deviate from the linear field behavior. All the resonance fields are plotted in the frequency-field diagram, presented in Fig. 7. Since a zero-field gap of ~20 GHz corresponds to the energy scale of H_{SF}, those resonance fields suggest conventional AF resonance modes in an anisotropic two-sublattice model [19,29,32–34]. Although the magnetic anisotropy in organic radical systems is known to be quite small, the anisotropic energy derived from the dipole-dipole interactions accompanying the phase transition to the LRO can induce more significant magnetic anisotropy [9,29].

Taking the experimental conditions of $T \ll 10$ K and $H < 4$ T, we then analyzed the experimental results in terms of a mean-field approximation assuming an $S = 2$ AF chain with on-site biaxial anisotropy. Thus, the spin Hamiltonian is expressed as

$$\mathcal{H} = J_{\mathrm{AF}} \sum_i \boldsymbol{S}_i \cdot \boldsymbol{S}_{2i-1} + D \sum_i \left(S_i^z\right)^2 + E \sum_i \left\{\left(S_i^x\right)^2 - \left(S_i^y\right)^2\right\} - g\mu_B \sum_i \boldsymbol{S}_i \cdot \boldsymbol{H}, \quad (2)$$

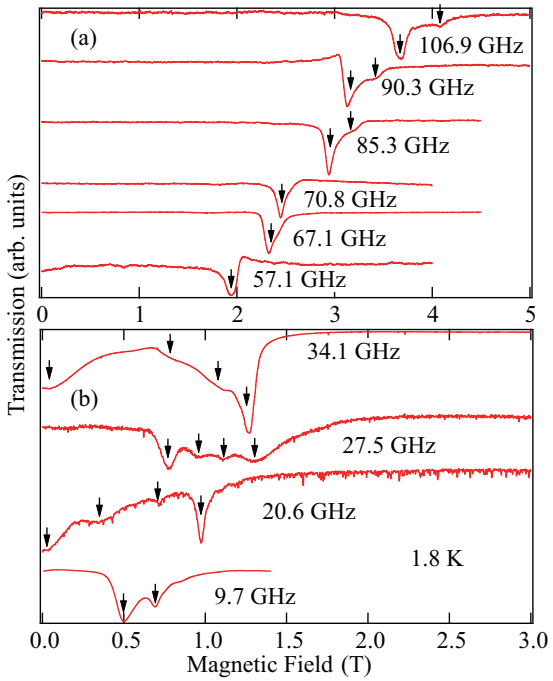

FIG. 6. Frequency dependence of ESR absorption spectra of (*o*-MePy-V)$FeCl_4$ at 1.8 K for (a) directly detected high frequencies and (b) low frequencies measured by cylindrical high-sensitivity cavities. The arrows indicate resonance signals.

where D and E are on-site anisotropies ($D, E < 0$), and $\boldsymbol{S}$ is an $S = 2$ spin operator. As the spin structure is described by a two-sublattice model, the free energy F is expressed in the following form, using the mean-field approximation:

$$F = A\boldsymbol{M}_1 \cdot \boldsymbol{M}_2 + K\left\{\left(M_1^z\right)^2 + \left(M_2^z\right)^2\right\} + L\left\{\left(M_1^x\right)^2 + \left(M_2^x\right)^2 - \left(M_1^y\right)^2 - \left(M_2^y\right)^2\right\} - (\boldsymbol{M}_1 + \boldsymbol{M}_2) \cdot \boldsymbol{H}, \quad (3)$$

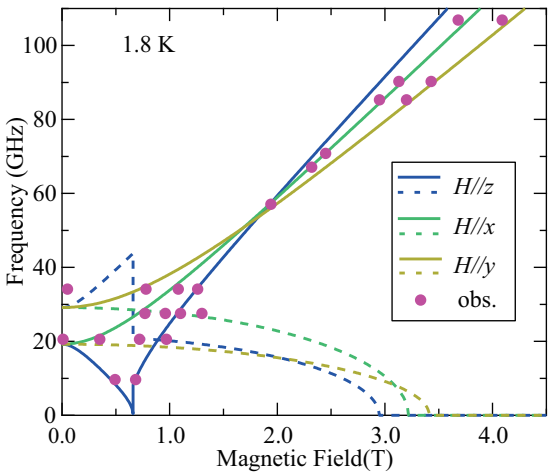

FIG. 7. Frequency-field plot of the ESR resonance fields at 1.8 K. The solid and broken lines are calculated AF resonance modes for the principal axes with high and low transition probabilities, respectively. The discontinuous changes of the lines correspond to the spin-flop transition at H_s.

where A, K, and L are given by

$$A = \frac{2}{N}\frac{2J_{\mathrm{AF}}}{(g\mu_B)^2}, \quad K = \frac{2}{N}\frac{D}{(g\mu_B)^2}, \quad L = \frac{2}{N}\frac{E}{(g\mu_B)^2}, \tag{4}$$

and $\boldsymbol{M}_1$ and $\boldsymbol{M}_2$ are the sublattice moments expressed as

$$\boldsymbol{M}_i = \frac{N}{2} g\mu_B \boldsymbol{S}_i. \tag{5}$$

Here, N is the number of hybrid spins, and $\boldsymbol{S}_i$ is the spin on the ith sublattice ($i = 1,2$). We derive the resonance conditions by solving the equation of motion

$$\partial \boldsymbol{M}_i/\partial t = \gamma[\boldsymbol{M}_i \times \boldsymbol{H}_i], \tag{6}$$

where γ is the gyromagnetic ratio and $\boldsymbol{H}_i$ is the mean field applied on the ith sublattice moment given by

$$\boldsymbol{H}_i = -\partial F/\partial \boldsymbol{M}_i. \tag{7}$$

To solve the equation of motion, we use a method for the analysis of ABX_3-type antiferromagnets [35]. Assuming precession motion of the sublattice moments around those equilibrium directions, we utilize the following expressions, which represent the motion of the ith sublattice moment:

$$\boldsymbol{M}_i = (\Delta M_{i\acute{x}} \exp(i\omega t), \Delta M_{i\acute{y}} \exp(i\omega t), |\boldsymbol{M}_i|), \tag{8}$$

where $\Delta M_{i\acute{x}}, \Delta M_{i\acute{y}} \ll |\boldsymbol{M}_i|$, and $\acute{x}$, $\acute{y}$, and $\acute{z}$ are the principal axes of the coordinate system on each sublattice moment. The $\acute{z}$ axis is defined as being parallel to the direction of each sublattice moment, and the $\acute{x}$ and $\acute{y}$ axes are perpendicular to the $\acute{z}$ axis.

The spins are aligned along the easy axis (z axis) under zero-field conditions, and the discontinuous spin-flop phase transition occurs at H_{SF} for $H \| z$. The value of H_{SF} is expressed as

$$H_{\mathrm{SF}} = \frac{4\sqrt{-D+E}\sqrt{D-E+2J_{\mathrm{AF}}}}{g\mu_B}, \tag{9}$$

which corresponds to the lowest zero-field energy gap of resonance modes. Above H_s, the two sublattices are tilted with respect to the field direction with equivalent angles, while for the other principal axes, where the external fields are applied perpendicular to the easy axis, the two sublattices are tilted from the easy axis with equivalent angles along each field direction. The angles between the sublattice moment and the external field for both directions can then be determined by minimizing the free energy. Then, the ω values are obtained by solving Eq. (6) numerically. The calculated results obtained here demonstrate typical AF resonance modes with biaxial anisotropy in a two-sublattice model. Since our experiments were performed using small, randomly oriented single crystals, the resonance fields for all of the principal axes are expected to have been detected in our experiments. As shown in Fig. 7, we obtain a good fit between the experimental and calculated values with the following parameters: $J_{\mathrm{AF}}/k_{\mathrm{B}} = 0.52$ K, $D/k_{\mathrm{B}} = -0.079$ K, and $E/k_{\mathrm{B}} = -0.033$ K. We note that for $H \| z$, the calculated lowest-frequency mode becomes soft and exhibits a discontinuous change at H_{SF}. For each field direction, the calculated gapped mode exhibits a gradual decrease with increasing field and becomes soft at each saturation field of about 3–3.5 T. These saturation fields coincide with the initial field of the 2/3 magnetization step as expected from our picture.

IV. SUMMARY

We have succeeded in synthesizing single crystals of the verdazyl-based charge-transfer salt (o-MePy-V)$FeCl_4$. *Ab initio* MO calculations indicated the formation of a partially stacked 2D spin model composed of five types of exchange interactions between $S_{\mathrm{V}} = 1/2$ and $S_{\mathrm{Fe}} = 5/2$ spins. The magnetic properties of the synthesized crystals indicate that the dominant AF interactions between the S_{V} and S_{Fe} spins stabilize an $S_{\mathrm{hy}} = 2$ spin at low temperatures, and that an effective $S = 2$ AF chain is formed for $T \ll 10$ K and $H < 4$ T. The resulting magnetization curve was explained using a classical MC method based on the $S = 2$ AF chain. The ESR resonance modes were also well explained by a mean-field analysis considering on-site biaxial anisotropy. Consequently, we evaluated magnetic parameters of the effective $S = 2$ AF chain as follows: $J_{\mathrm{AF}}/k_{\mathrm{B}} = 0.52$ K, $D/k_{\mathrm{B}} = -0.079$ K, and $E/k_{\mathrm{B}} = -0.033$ K. At higher fields, the magnetization exhibited two-thirds of the full saturation for fields between 4 and 20 T, before approaching saturation at approximately 40 T. The effective spin model in the high-field region is considered to be a three-dimensionally coupled $S_{\mathrm{V}} = 1/2$ honeycomb lattice with an effective internal field arising from the S_{Fe} spins. These results thus demonstrate the realization of an $S = 2$ AF chain through the metal-radical hybrid spin in the newly synthesized salt (o-MePy-V)$FeCl_4$.

ACKNOWLEDGMENTS

This research was partly supported by Grant for Basic Science Research Projects from KAKENHI (Grants No. 15H03695, No. 15K05171, and No. 17H04850) and the CASIO Science Promotion Foundation. A part of this work was carried out at the Center for Advanced High Magnetic Field Science in Osaka University under the Visiting Researcher's Program of the Institute for Solid State Physics, the University of Tokyo, and the Institute for Molecular Science.

[1] M. Takahashi, P. Turek, Y. Nakazawa, M. Tamura, K. Nozawa, D. Shiomi, M. Ishikawa, and M. Kinoshita, Phys. Rev. Lett. **67**, 746 (1991).

[2] E. V. Tretyakov and V. I. Ovcharenko, Russ. Chem. Rev. **78**, 971 (2009).

[3] H. Yamaguchi, K. Iwase, T. Ono, T. Shimokawa, H. Nakano, Y. Shimura, N. Kase, S. Kittaka, T. Sakakibara, T. Kawakami, and Y. Hosokoshi, Phys. Rev. Lett. **110**, 157205 (2013).

[4] H. Yamaguchi, H. Miyagai, T. Shimokawa, K. Iwase, T. Ono, Y. Kono, N. Kase, K. Araki, S. Kittaka, T. Sakakibara, T.

Kawakami, K. Okunishi, and Y. Hosokoshi, J. Phys. Soc. Jpn. **83**, 033707 (2014).
[5] H. Yamaguchi, T. Okubo, K. Iwase, T. Ono, Y. Kono, S. Kittaka, T. Sakakibara, A. Matsuo, K. Kindo, and Y. Hosokoshi, Phys. Rev. B **88**, 174410 (2013).
[6] H. Yamaguchi, T. Okubo, S. Kittaka, T. Sakakibara, K. Araki, K. Iwase, N. Amaya, T. Ono, and Y. Hosokoshi, Sci. Rep. **5**, 15327 (2015).
[7] H. Yamaguchi, M. Okada, Y. Kono, S. Kittaka, T. Sakakibara, T. Okabe, Y. Iwasaki, and Y. Hosokoshi, Sci. Rep. **7**, 16144 (2017).
[8] H. Yamaguchi, Y. Shinpuku, T. Shimokawa, K. Iwase, T. Ono, Y. Kono, S. Kittaka, T. Sakakibara, and Y. Hosokoshi, Phys. Rev. B **91**, 085117 (2015).
[9] H. Yamaguchi, Y. Shinpuku, Y. Kono, S. Kittaka, T. Sakakibara, M. Hagiwara, T. Kawakami, K. Iwase, T. Ono, and Y. Hosokoshi, Phys. Rev. B **93**, 115145 (2016).
[10] F. D. M. Haldane, Phys. Rev. Lett. **50**, 1153 (1983).
[11] S. Todo and K. Kato, Phys. Rev. Lett. **87**, 047203 (2001).
[12] H. Nakano and A. Terai, J. Phys. Soc. Jpn. **78**, 014003 (2009).
[13] K. Katsumata, H. Hori, T. Takeuchi, M. Date, A. Yamagishi, and J. P. Renard, Phys. Rev. Lett. **63**, 86 (1989).
[14] I. A. Zaliznyak, S.-H. Lee, and S. V. Petrov, Phys. Rev. Lett. **87**, 017202 (2001).
[15] I. Affleck, T. Kennedy, E. H. Lieb, and H. Tasaki, Phys. Rev. Lett. **59**, 799 (1987).
[16] M. Hagiwara, K. Katsumata, I. Affleck, B. I. Halperin, and J. P. Renard, Phys. Rev. Lett. **65**, 3181 (1990).
[17] S. Itoh, H. Tanaka, and M. J. Bull, J. Phys. Soc. Jpn. **71**, 1148 (2002).
[18] G. E. Granroth, M. W. Meisel, M. Chaparala, Th. Jolicoeur, B. H. Ward, and D. R. Talham, Phys. Rev. Lett. **77**, 1616 (1996).
[19] S.-i. Shinozaki, A. Okutani, D. Yoshizawa, T. Kida, T. Takeuchi, S. Yamamoto, O. N. Risset, D. R. Talham, M. W. Meisel, and M. Hagiwara, Phys. Rev. B **93**, 014407 (2016).
[20] C. Stock, L. C. Chapon, O. Adamopoulos, A. Lappas, M. Giot, J. W. Taylor, M. A. Green, C. M. Brown, and P. G. Radaelli, Phys. Rev. Lett. **103**, 077202 (2009).
[21] T. Birk, K. S. Pedersen, S. Piligkos, C. Aa. Thuesen, H. Weihe, and J. Bendix, Inorg. Chem. **50**, 5312 (2011).
[22] M. B. Stone, G. Ehlers, and G. E. Granroth, Phys. Rev. B **88**, 104413 (2013).
[23] S. Itho, T. Yokoo, S. Yano, D. Kawana, H. Tanaka, and Y. Endoh, J. Phys. Soc. Jpn. **81**, 084706 (2012).
[24] R. Kuhn, Angew. Chem. **76**, 691 (1964).
[25] K. Mukai, S. Jinno, Y. Shimobe, N. Azuma, M. Taniguchi, Y. Misaki, K. Tanaka, K. Inoue, and Y. Hosokoshi, J. Mater. Chem. **13**, 1614 (2003).
[26] M. Shoji, K. Koizumi, Y. Kitagawa, T. Kawakami, S. Yamanaka, M. Okumura, and K. Yamaguchi, Chem. Phys. Lett. **432**, 343 (2006).
[27] H. Yamaguchi, A. Toho, K. Iwase, T. Ono, T. Kawakami, T. Shimokawa, A. Matsuo, and Y. Hosokoshi, J. Phys. Soc. Jpn. **82**, 043713 (2013).
[28] T. Okabe, H. Yamaguchi, S. Kittaka, T. Sakakibara, T. Ono, and Y. Hosokoshi, Phys. Rev. B **95**, 075120 (2017).
[29] H. Yamaguchi, Y. Tamekuni, Y. Iwasaki, R. Otsuka, Y. Hosokoshi, T. Kida, and M. Hagiwara, Phys. Rev. B **95**, 235135 (2017).
[30] K. Kopinga, T. de Neef, W. J. M. de Jonge, and B. C. Gerstein, Phys. Rev. B **13**, 3953 (1976).
[31] J. L. Manson, Q. Huang, J. W. Lynn, H. Koo, M. Whangbo, R. Bateman, T. Otsuka, N. Wada, D. Argyriou, and J. Miller, J. Am. Chem. Soc. **123**, 162 (2001).
[32] C. Kittel, Phys. Rev. **82**, 565 (1951).
[33] M. Hagiwara, K. Katsumata, I. Yamada, and H. Suzuki, J. Phys.: Condens. Matter **8**, 7349 (1996).
[34] R. S. Fishman, S.-i. Shinozaki, A. Okutani, D. Yoshizawa, T. Kida, M. Hagiwara, and M. W. Meisel, Phys. Rev. B **94**, 104435 (2016).
[35] H. Tanaka, Y. Kaahwa, T. Hasegawa, M. Igarashi, S. Teraoka, K. Iio, and K. Nagata, J. Phys. Soc. Jpn. **58**, 2930 (1989).